

Violation of universality in anomalous Fourier's law

Pablo I. Hurtado* and Pedro L. Garrido†

Institute Carlos I for Theoretical and Computational Physics and Departamento de Electromagnetismo y Física de la Materia, Universidad de Granada, 18071 Granada, Spain

(Dated: June 11, 2015)

Since the discovery of long-time tails, it has been clear that Fourier's law in low dimensions is typically anomalous, with a size-dependent heat conductivity, though the nature of the anomaly remains puzzling. The conventional wisdom, supported by recent results from nonlinear fluctuating hydrodynamics, is that the anomaly is universal in $1d$ momentum-conserving systems and belongs in the Kardar-Parisi-Zhang universality class. Here we challenge this picture by using a novel scaling method to show unambiguously that universality breaks down in the paradigmatic $1d$ diatomic hard-point fluid. Hydrodynamic profiles for a broad set of gradients, densities and sizes all collapse onto an universal master curve, showing that (anomalous) Fourier's law holds even deep into the nonlinear regime. This allows to solve the macroscopic transport problem for this model, a solution which compares flawlessly with data and, interestingly, implies the existence of a bound on the heat current in terms of pressure. These results question the use of standard fluctuating hydrodynamics to understand anomalous Fourier's law in $1d$, offering a new perspective on transport and its anomalies in low dimensions.

PACS numbers: 44.10.+i, 05.40.-a, 05.70.Ln, 65.20.-w

INTRODUCTION

It's going to be 200 years since Fourier stated his seminal law [1], but its microscopic understanding still poses one of the most important and challenging open problems in nonequilibrium statistical physics, with no rigorous mathematical derivation to date [2–6]. Fourier's law establishes the proportionality between the heat current and the local temperature gradient in a material, with the proportionality factor defining the heat conductivity κ , a key material property. While for bulk, three-dimensional materials κ is well characterized and measured, its status in low-dimensional structures is far from clear. In particular, for low-dimensional systems ($d = 1, 2$) with momentum conservation, κ grows with the system size L , diverging in the thermodynamic limit and thus leading to anomalous heat transport [3–6]. The understanding of this anomaly has attracted a lot of attention in recent years [3–39], not only because it is expected to shed light on the key ingredients behind Fourier's law at a fundamental level, but also because of its technological relevance in low-dimensional real-world materials, the most noteworthy being graphene [7–10], but with other important examples ranging from molecular chains [11] and carbon nanotubes [12] to polymer fibers [13, 14], nanowires [15, 16] and even spider silk [17], to mention just a few; see [6] for a recent review. From a theoretical perspective, the low-dimensional anomaly in heat transport can be linked to the presence of strong dynamic correlations (or long-time tails) in fluids and lattices [18–20], though a detailed understanding has remained elusive for decades. The prevailing picture, however, is that anomalous heat transport in $1d$ momentum-conserving systems is *universal* and within the Kardar-Parisi-Zhang (KPZ) universality class [3–6], an idea rein-

forced by recent breakthroughs from *nonlinear* fluctuating hydrodynamics (nFH) [21–27]. In particular, $\kappa \sim L^\alpha$ with $\alpha = 1/3$ is expected in the general case, though a second universality class with $\alpha = 1/2$ appears under special circumstances (as e.g. for zero-pressure systems [22, 28–32]); see also [40].

Here we challenge this picture by using a novel scaling method to offer a high-precision measurement of the conductivity anomaly exponent in a paradigmatic $1d$ model of transport. Compared to previous attempts at measuring the anomaly exponent, most based on *linear* response theory and hence critically-dependent on a large system-size limit (which is in fact never attained) [37], our method takes full advantage of the *nonlinear* character of the heat conduction problem in a natural way, accounting with striking simplicity for all finite-size effects. Our model is the archetypical $1d$ diatomic hard-point gas in a temperature gradient [44–53], which is characterized by the mass ratio $\mu = M/m > 1$ between neighboring particles. We unambiguously show below that, contrary to the standard lore, this model does obey (anomalous) Fourier's law for a broad range of temperature gradients, even deep into the nonlinear regime, in the sense that the heat current J is proportional to the local temperature gradient,

$$J = -\kappa_L(\rho, T) \frac{dT(x)}{dx}, \quad (1)$$

with a well-defined local conductivity functional $\kappa_L(\rho, T) = L^\alpha \sqrt{T/m} k(\rho)$. This is proven by collapsing onto a striking universal master curve the density and temperature profiles measured for a large set of system sizes, number densities and temperature gradients. Such compelling collapse offers a high-precision measurement of the anomaly exponent α , which remarkably turns out

to be *non-universal*, depending non-monotonously on the mass ratio μ . This surprising but clear-cut result hence signals the breakdown of the universality claimed for $1d$ anomalous Fourier's law on the basis of nFH. The observed scaling allows to solve the macroscopic transport problem for this model, and we obtain analytic expressions for the universal master curve (and the hydrodynamic profiles) which exhibit an excellent agreement with measurements. Interestingly, this solution immediately implies the existence of a nontrivial bound on the heat current in terms of the pressure P . All together, these results offer a completely new and surprising perspective on transport and its anomalies in low dimensions, opening new avenues of research.

RESULTS

We hence consider a $1d$ Hamiltonian model fluid consisting in N hard-point particles with alternating masses, $m = 1$ and $M = \mu m > 1$, moving ballistically in a line of length L in between elastic collisions with neighboring particles. The fluid is coupled to two stochastic thermal walls [3–5] at the boundaries, $x = 0, L$, operating at different temperatures $T_0 > T_L = 1$ and thus driving the system to an inhomogeneous nonequilibrium steady state characterized by nonlinear density and temperature profiles, $\rho(x)$ and $T(x)$ respectively [3–6]. Interestingly, these profiles can be shown to follow from an universal master curve [33], independent of the driving gradient and the fluid's density, provided that (i) Fourier's law (1) and (ii) macroscopic local equilibrium (MLE) hold (see Appendix A), a general result valid for arbitrary d -dimensional fluids and confirmed in simulations of hard disks [33], which also holds in the reverse direction. MLE implies that the stationary density and temperature fields are locally coupled via the equilibrium equation of state (EoS) [54], which for the $1d$ diatomic hard-point fluid simply takes the form of the ideal gas EoS, $P = \rho T$. In this way, iff hypotheses (i)-(ii) hold, together with the scaling ansatz (iii) $\kappa_L(\rho, T) = L^\alpha \sqrt{T/m} k(\rho)$, we expect all density and temperature profiles to scale as

$$\rho(x) = F\left(\frac{\psi x}{L^\alpha} + \zeta\right) \quad ; \quad \frac{T(x)}{P} = 1/F\left(\frac{\psi x}{L^\alpha} + \zeta\right) \quad (2)$$

with $\psi = J\sqrt{m}/P^{3/2}$ the reduced current and ζ a constant, see Appendix A. This scaling defines an universal master curve $F(u)$ from which all profiles follow. Alternatively, Eq. (2) implies that all measured density and temperature profiles can be collapsed onto an universal master curve after appropriately scaling space by $L^{-\alpha}\psi$, with ψ measured in each case, and shifting the curve by a constant ζ . The resulting collapse is expected to be very sensitive to the anomaly exponent α , and this suggests a simple scaling procedure to measure both α and the

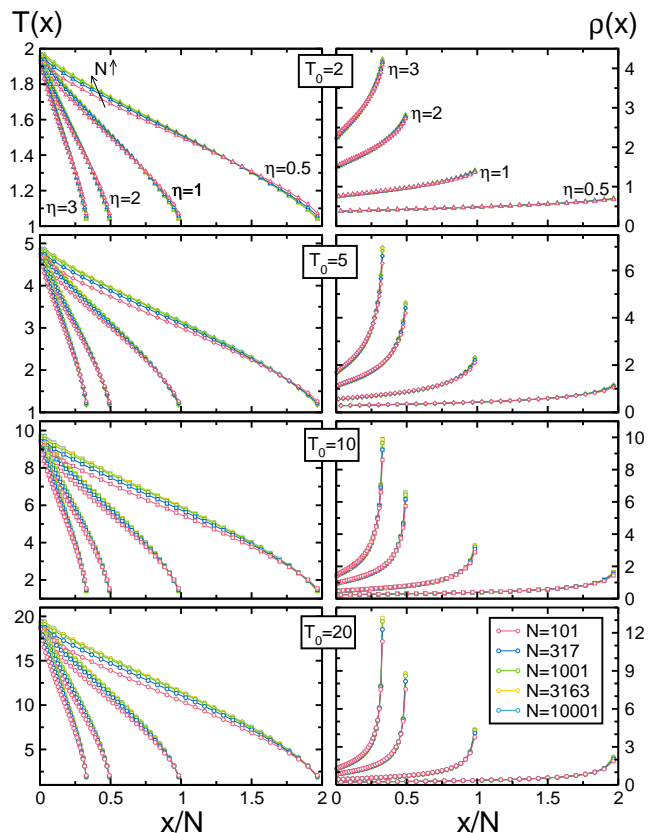


FIG. 1. (Color online) Temperature (left) and density (right) profiles measured for (from top to bottom) $T_0 = 2, 5, 10, 20$ and varying η and N , for a mass ratio $\mu = 3$.

universal master curve in simulations, confirming at the same time our starting hypotheses.

In order to do so, we performed a large number of event-driven simulations of the $1d$ diatomic gas for a broad set of boundary temperatures $T_0 = 2, 5, 10, 20$ (with fixed $T_L = 1$), global number densities $\eta \equiv N/L = 0.5, 1, 2, 3$, numbers of particles $N = 101, 317, 1001, 3163, 10001$, and different mass ratios $\mu = 1.3, 1.618, 2.2, 3, 5, 10, 30, 100$. We measured locally a number of relevant observables including the local kinetic energy, number density, virial pressure and energy current density, as well as the energy current flowing through the thermal reservoirs at $x = 0, L$ and the pressure exerted on these walls. We stress that observables measured at the walls agree in all cases with their bulk counterparts, which are constant along the system. For local measurements, we divided the fluid in 30 virtual cells, a constant number independent of other system parameters. The simulation time unit was set to $t_0 = \sqrt{M/(2T_L\eta^2)}$, the mean free time of a heavy particle in a cool environment, and time averages were performed every $10t_0$ for a total time of $(10^8 - 10^9)t_0$, after a relaxation time of 10^3t_0 which empirically guarantees relaxation to the steady state. Statistical errors are computed in all cases at 99.7% confidence level, and error

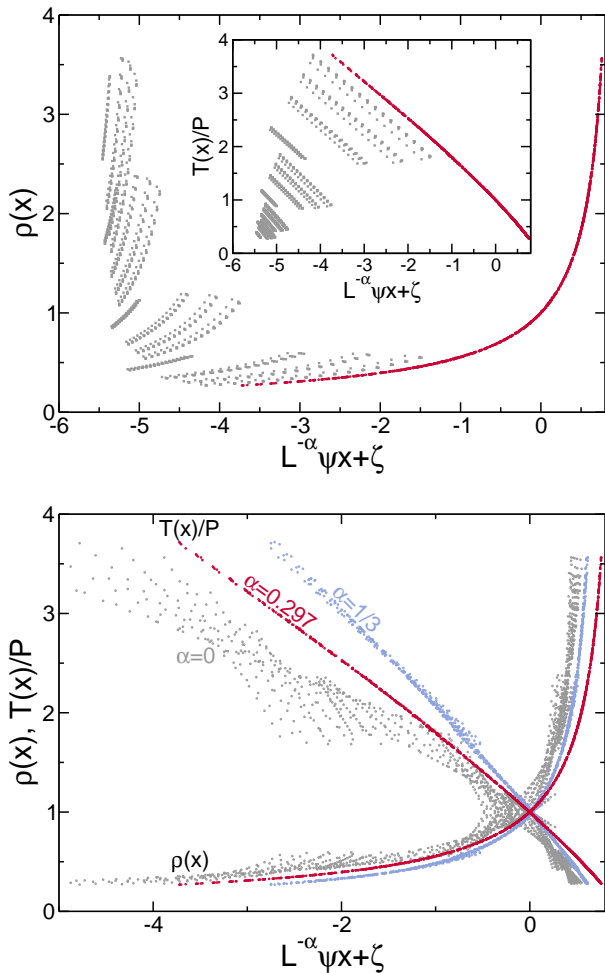


FIG. 2. (Color online) Top: Density profiles for $\mu = 3 \forall N, T_0, \eta$ as a function of $L^{-\alpha}\psi x$ with $\alpha = 0.297$, before (light gray) and after (dark red) the shifts ζ . Inset: Same as before, but for the reduced temperature profiles. Note that the shifts are those obtained from density profiles. In both cases the data collapse is remarkable. Bottom: Optimal collapse of density and reduced temperature profiles for $\mu = 3$ and three different exponents $\alpha = 0, 0.297$, and $1/3$. The superior collapse for $\alpha = 0.297$ is apparent. The abscissa for $\alpha = 0$ has been divided by a factor 10 for the sake of clarity.

bars are shown if larger than the plotted symbols. Fig. 1 shows the temperature and density profiles measured for $\mu = 3$ and varying T_0, η and N (similar data are obtained for all other μ 's). These profiles are clearly non-linear, and exhibit strong finite-size effects. However, the measured local density and temperature in each case are tightly coupled by the equilibrium EoS, $P = \rho(x)T(x)$, with P the finite-size pressure measured in each simulation, see Appendix B, validating hypothesis (ii) above and confirming the robustness of MLE far from equilibrium [54]. Note that the thermal walls act as defects (akin to fixed, infinite-mass particles) which disrupt the structure of the surrounding fluid, defining two boundary layers where finite-size corrections mount up. To an-

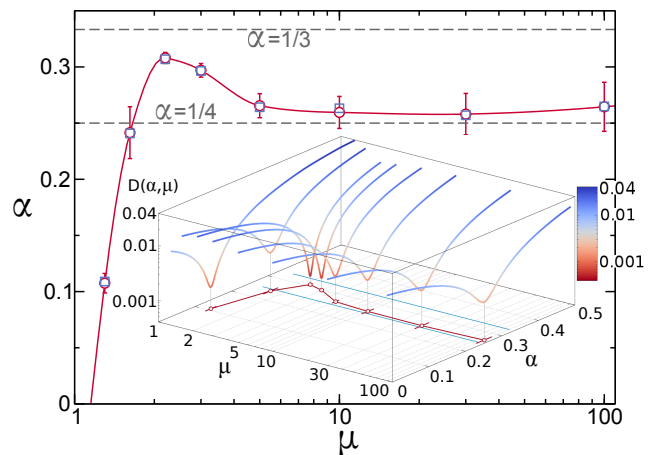


FIG. 3. (Color online) Mass ratio dependence of the anomaly exponent measured from scaling (\circ). The non-monotonous behavior of α vs μ clearly signals the breakdown of universality for anomalous Fourier's law in 1d. The exponent measured from the power-law fit for $k(\rho)$ is also shown (\square), see Fig. 5, being fully compatible with the measured α in each case. The line is a guide to the eye. Inset: The collapse metric $D(\alpha, \mu)$ as a function of α exhibits a deep and narrow minimum for each μ (notice the logarithmic scale in z -axis), offering a precise measurement of the anomaly exponent and its error.

alyze below the fluid's scaling behavior, we neglect data from these boundary layers (up to 7 cells adjacent to each wall), focusing the analysis on the remaining *bulk* profiles $\rho(x)$ and $T(x)$. For a given exponent α , each bulk density profile $\rho(x)$ is then plotted as a function of $L^{-\alpha}\psi x$ (with $\psi = J\sqrt{m}/P^{3/2}$ measured in each case, see Appendix B), and shifted by a constant ζ to achieve an optimal collapse among all scaled profiles, see top panel in Fig. 2. The vector of optimal shifts ζ_0 for fixed α and μ is obtained by minimizing a standard collapse metric $D(\zeta; \alpha, \mu)$ for the density profiles, see Appendix C, which roughly speaking measures the relative average distance among all pairs of overlapping curves [55], and the same shifts are used to collapse reduced temperature profiles, $T(x)/P$. The resulting data collapses are very sensitive to α , see bottom panel in Fig. 2, so the true anomaly exponent α can be measured with high precision for each mass ratio μ by minimizing $D(\alpha, \mu) \equiv D(\zeta_0; \alpha, \mu)$ as a function of α . In fact, the distance function $D(\alpha, \mu)$ has a pronounced minimum in α for each μ , see inset in Fig. 3, whose width and depth allow to estimate the exponent error, see Appendix C. Remarkably, the measured anomaly exponent is *non-universal*, depending non-monotonously on the mass ratio, $\alpha = \alpha(\mu)$, see main panel in Fig. 3 and Table I in Appendix B, growing first from small values at low μ to a maximum $\alpha \approx 0.3 < 1/3$ for $\mu = 2.2$, and decaying afterwards to an asymptotic value $\alpha \approx 1/4$ for large μ . Fig. 4 shows the master curves obtained from density and reduced temperature bulk profiles for different μ 's by using the measured exponent α in each

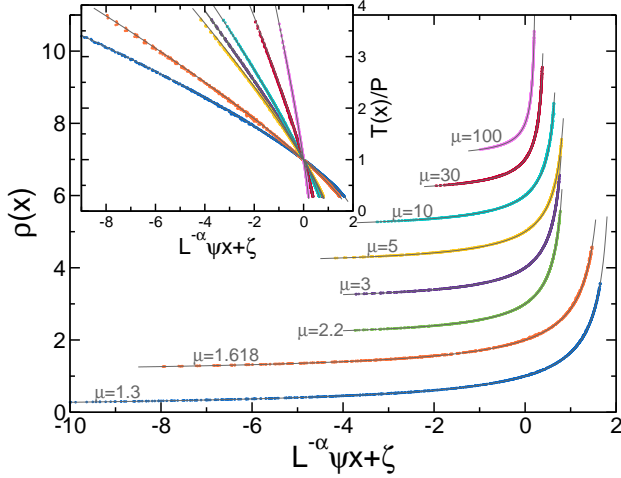


FIG. 4. (Color online) Main: Collapse of density profiles for each μ obtained by using the measured α in each case, see Fig. 3. The master curves have been shifted vertically for better comparison. In all cases, the data collapse is excellent. The lines are theoretical predictions, see main text. Inset: Collapse of reduced temperature profiles for the same conditions, and theoretical curves. In all cases, each curve for fixed μ contains 1280 points measured in 80 different simulations for varying N , T_0 and η . The abscisas for the $\mu = 1.3$ data have been divided by 4 to better visualize the results.

case, and in all cases the resulting collapses are impressive, confirming that Fourier's law (1) rules heat transport in this 1d model. Moreover, this surprising but unambiguous result also calls into question the prevailing idea that the anomaly in 1d heat transport is universal, a claim compatible with recent results from nFH [21–28]. We discuss below a plausible origin for such universality breakdown [27, 34, 35].

We next focus on the density dependence of the heat conductivity $\kappa_L(\rho, T) = L^\alpha \sqrt{T/mk(\rho)}$. Interestingly, the dynamics of 1d hard-point fluids remains invariant under different scalings (of temperature, velocities, space, mass, etc.) [5]. Using such invariance, it is easy to show rigorously that $\kappa_L(\rho, T) = \sqrt{T/m} f(N, \mu)$, with f some adimensional function of N and μ . This in turn implies, via dimensional analysis, that necessarily $k(\rho) = a\rho^\alpha$, with a some constant. This is fully confirmed in local measurements of the density dependence of the heat conductivity, from which we determine $a = a(\mu)$, see Appendix B and Table I therein. This observation opens the door to a full solution of the macroscopic heat transport problem for this model, see Appendix A. In particular, the universal master curve $F(u)$ of Eq. (2) is $F(u) = (1 - u/\nu^*)^{2/(2\alpha-3)}$, with $\nu^* \equiv a/(\frac{3}{2} - \alpha)$. This master curve depends on μ through the mass ratio dependence of α and a . Fig. 4 displays the predicted master curves, with the only input of the measured $\alpha(\mu)$ and $a(\mu)$, and the agreement with collapsed data is stunning.

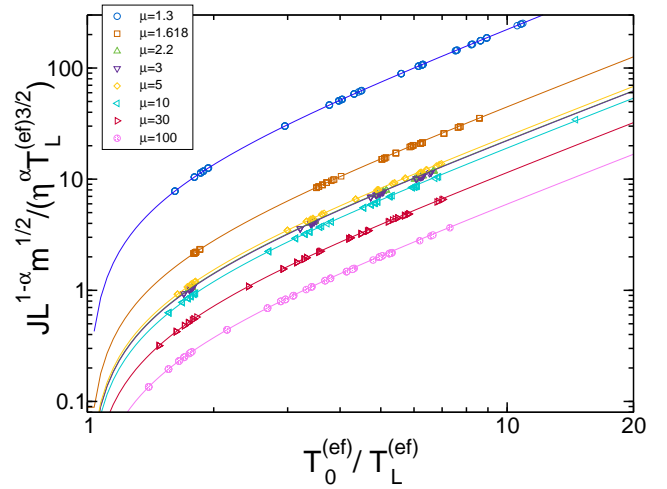


FIG. 5. (Color online) Test of the macroscopic theory prediction for the heat current, see Eqs. (16)-(17) in Appendix A. For each μ , $JL^{1-\alpha}\sqrt{m}/(\eta^\alpha T_L^{(\text{ef})3/2})$ is plotted vs $T_0^{(\text{ef})}/T_L^{(\text{ef})}$, with J the measured current, and $T_{0,L}^{(\text{ef})}$ the effective boundary temperatures for bulk profiles measured in each case. The agreement between data and theory is excellent in all cases.

Closed forms for temperature profiles follow as

$$T(x) = \left[T_0^{\frac{3}{2}-\alpha} - \frac{J\sqrt{m}}{\nu^* P^\alpha} L^{-\alpha} x \right]^{\frac{2}{3-2\alpha}}, \quad x \in [0, L], \quad (3)$$

with density profiles given as $\rho(x) = P/T(x)$, and P and J simply written in terms of external parameters T_0 , T_L , η , and L , see Appendix A. Note that this novel macroscopic solution is compatible with known scaling symmetries of 1d hard-point fluids [5]. Interestingly, the master curve $F(u)$ exhibits a vertical asymptote at $u = \nu^*$, and this immediately implies the existence of a bound on the scaled current in terms of pressure, $L^{1-\alpha} J \leq \nu^* T_0^{3/2-\alpha} P^\alpha / \sqrt{m} \forall T_0, T_L, \eta, L$, see also Eq. (3).

Eq. (3) can be readily tested against data, see Appendix B, confirming that the bulk $T(x)^{3/2-\alpha}$ is linear in x with slope $-JL^{-\alpha}\sqrt{m}/(\nu^* P^\alpha)$, with J and P measured in each case, but with effective boundary temperatures slightly different from the thermal wall temperatures in each case, $T_{0,L}^{(\text{ef})} \neq T_{0,L}$. This shows that the measured *bulk* temperature (and density) profiles for any finite N are in fact those of a *macroscopic* diatomic hard-point gas obeying (1) but subject to some effective, N -dependent boundary conditions controlled by the boundary layers. Indeed, the striking collapse of data and the agreement with the macroscopic master curve in Fig. 4 strongly support this conclusion. This is a manifestation of the bulk-boundary decoupling phenomenon already reported in hard disks out of equilibrium [33], which enforces the macroscopic laws on the bulk of the finite-sized fluid. Our macroscopic theory also offers a precise prediction for the heat current in terms of the external parameters, see Appendix A. In particular, it predicts that

$JL^{1-\alpha}\sqrt{m}/(\eta^\alpha T_L^{3/2})$ is a well-defined function of T_0/T_L . Fig. 5 tests this prediction against data, using the effective boundary temperatures $T_{0,L}^{(ef)}$ measured above, and the agreement is excellent $\forall N, T_0, \eta$ for each μ .

DISCUSSION

Some comments are now in order. The excellent collapse of our data confirms that Fourier's law (1) holds in this model with a well-defined (albeit size-dependent) local conductivity functional $\kappa_L(\rho, T) = a(\rho L)^\alpha \sqrt{T/m}$. This is true even for finite N (as small as $\mathcal{O}(10^2)$!) and under large temperature gradients, extending the range of validity of (anomalous) Fourier's law deep into the non-linear regime and evidencing the absence of higher-order (Burnett-like) corrections in $1d$ [33]. Furthermore, we provide strong evidence supporting the breakdown of universality in anomalous Fourier's law for $1d$ momentum-conserving systems. This shows that the universality observed in the spatiotemporal propagation of equilibrium fluctuations in $1d$, predicted by nFH and tested in simulations [22–27], does not carry over however to the heat conductivity anomaly in $1d$ nonequilibrium steady states. The universality breakdown reported in this work may hint at a possible existence of hidden conservation laws in the diatomic hard-point gas and hence further slow-evolving fields beyond the standard hydrodynamic ones. Such intriguing behavior has been already reported in the nonequilibrium response of this model to a shock wave excitation [34, 35]. Moreover, as recently suggested [27], the existence of further conservation laws may give rise to an infinite discrete (Fibonacci) family of anomaly exponents that can coexist in different regions of parameter space for a given model [27], a behavior reminiscent of our results. The question remains as to how to reconcile the local nature of Fourier's law with the non-local L^α -term in $\kappa_L(\rho, T)$. Our data suggest that this could be achieved in a nonlinear fluctuating hydrodynamics description of the problem derived via an anomalous, non-diffusive hydrodynamic scaling of microscopic spatiotemporal variables, $x \rightarrow x/L^{1-\alpha}$ and $t \rightarrow t/L^{2-3\alpha}$ [56]. We also mention that recent results suggest yet another mesoscopic description of anomalous transport in $1d$ in terms of fractional diffusion equations and/or heat carriers with Lévy-walk statistics [57–60]. As far as we know, this description does not seem compatible with the scaling and data collapses observed in this work.

The scaling method here used can be implemented to study transport in any type of fluid or lattice system in arbitrary dimension, offering a clean procedure to obtain asymptotic transport coefficients and hence opening the door to a deeper understanding of anomalous transport in low dimensions. In particular, this scaling method takes full advantage of the nonlinear character of the transport problem, accounting for all finite-size ef-

fects and avoiding additional hypotheses underlying the usual linear-response-based measurements, which lead to strong finite-size corrections [37], running effective exponents [53], etc. In this sense it would be interesting to apply a similar scaling analysis to other paradigmatic models of heat transport in low dimensions, as e.g. the Fermi-Pasta-Ulam model of anharmonic oscillators and the hard-square or -shoulder potentials [3–5], where the universality breakdown here reported can be further investigated. The role of conservative noise [59, 60] as a smoothing mechanism to get rid of non-hydrodynamic, hidden conservation laws should be also investigated.

We thank H. van Beijeren, A. Dhar, J.L. Lebowitz, J.J. del Pozo, and H. Spohn for useful discussions. Financial support from Spanish projects FIS2009-08451 (MICINN) and FIS2013-43201-P (MINECO), University of Granada, Junta de Andalucía projects P06-FQM1505, P09-FQM4682 and GENIL PYR-2012-1 and PYR-2014-13 projects is acknowledged.

* phurtado@onsager.ugr.es

† garrido@onsager.ugr.es

- [1] J. Fourier, *Théorie analytique de la chaleur* (1822).
- [2] J.L. Lebowitz, Nonequilibrium statistical physics today: Where shall we go from here?, AIP Conf. Proc. **1332**, 3 (2011).
- [3] F. Bonetto, J.L. Lebowitz, and L. Rey-Bellet, Fourier's law: A challenge to theorists, in *Mathematical Physics 2000*, A. Fokas, A. Grigoryan, T. Kibble, and B. Zegarlinski (eds.), Imperial College Press, London (2000), pp. 128-150.
- [4] S. Lepri, R. Livi, and A. Politi, Thermal conduction in classical low-dimensional lattices, Phys. Rep. **377**, 1 (2003).
- [5] A. Dhar, Heat transport in low-dimensional systems, Adv. Phys. **57**, 457 (2008).
- [6] S. Liu, X. Xu, R. Xie, G. Zhang, and B. Li, Anomalous heat conduction and anomalous diffusion in low dimensional nanoscale systems, Euro. Phys. J. B **85**, 337 (2012).
- [7] S. Ghosh, I. Calizo, D. Teweldebrhan, E.P. Pokatilov, D.L. Nika, A.A. Balandin, W. Bao, F. Miao, and C.N. Lau, Extremely high thermal conductivity of graphene: Prospects for thermal management applications in nanoelectronic circuits, Appl. Phys. Lett. **92**, 151911 (2008).
- [8] A.A. Balandin, S. Ghosh, W. Bao, I. Calizo, D. Teweldebrhan, F. Miao, and C.N. Lau, Superior thermal conductivity of single-layer graphene, Nano Lett. **8**, 902 (2008).
- [9] Ghosh, W. Bao, D.L. Nika, S. Subrina, E.P. Pokatilov, C.N. Lau, and A.A. Balandin, Dimensional crossover of thermal transport in few-layer graphene, Nature Materials **9**, 555 (2010).
- [10] A.A. Balandin, Thermal properties of graphene and nanostructured carbon materials, Nature Materials **10**, 569 (2011).
- [11] T. Meier, F. Menges, P. Nirmalraj, H. Hölscher, H. Riel, and B. Gotsmann, Length-dependent thermal transport

- along molecular chains, *Phys. Rev. Lett.* **113**, 060801 (2014).
- [12] C.W. Chang, D. Okawa, H. Garcia, A. Majumdar, and A. Zettl, Breakdown of Fourier's law in nanotube thermal conductors, *Phys. Rev. Lett.* **101**, 075903 (2008).
- [13] A. Henry, and G. Chen, High thermal conductivity of single polyethylene chains using molecular dynamics simulations, *Phys. Rev. Lett.* **101**, 235502 (2008).
- [14] J. Liu, and R. Yang, Length-dependent thermal conductivity of single extended polymer chains, *Phys. Rev. B* **86**, 104307 (2012).
- [15] T.-K. Hsiao, H.-K. Chang, S.-C. Liou, M.-W. Chu, S.-C. Lee, and C.-W. Chang, Observation of room-temperature ballistic thermal conduction persisting over $8.3 \mu\text{m}$ in SiGe nanowires, *Nature Nanotech.* **8**, 534 (2013).
- [16] N. Yang, G. Zhang, and B. Li, Violation of Fourier's law and anomalous heat diffusion in silicon nanowires, *Nano Today* **5**, 85-90 (2010).
- [17] X. Huang, G. Liu, and X. Wang, New secrets of spider silk: Exceptionally high thermal conductivity and its abnormal change under stretching, *Adv. Mater.* **24**, 1482 (2012).
- [18] B.J. Alder and T.E. Wainwright, Velocity autocorrelations for hard spheres, *Phys. Rev. Lett.* **18**, 988 (1967).
- [19] B.J. Alder and T.E. Wainwright, Decay of the velocity autocorrelation function, *Phys. Rev. A* **1**, 18 (1970).
- [20] P. Résibois and M. De Leener, *Classical kinetic theory of fluids*, John Wiley & Sons, New York (1977).
- [21] O. Narayan and S. Ramaswamy, Anomalous heat conduction in one-dimensional momentum conserving systems, *Phys. Rev. Lett.* **89**, 200601 (2002).
- [22] H. van Beijeren, Exact results for anomalous transport in one-dimensional hamiltonian systems, *Phys. Rev. Lett.* **108**, 180601 (2012).
- [23] C.B. Mendl, and H. Spohn, Dynamic correlators of Fermi-Pasta-Ulam chains and nonlinear fluctuating hydrodynamics, *Phys. Rev. Lett.* **111**, 230601 (2013).
- [24] H. Spohn, Nonlinear fluctuating hydrodynamics for anharmonic chains. *J. Stat. Phys.* **154**, 1191 (2014).
- [25] S.G. Das, A. Dhar, K. Saito, C.B. Mendl, and H. Spohn, Numerical test of hydrodynamic fluctuation theory in the Fermi-Pasta-Ulam chain, *Phys. Rev. E* **90**, 012124 (2014).
- [26] C.B. Mendl, and H. Spohn, Current fluctuations for anharmonic chains in thermal equilibrium. *J. Stat. Mech.* 03007 (2015).
- [27] V. Popkov, A. Schadschneider, J. Schmidt, and G.M. Schütz, The Fibonacci family of dynamical universality classes, arXiv:1505.04461 (2015).
- [28] G.R. Lee-Dadswell, Universality classes for thermal transport in one-dimensional oscillator systems, *Phys. Rev. E* **91**, 032102 (2015).
- [29] L. Delfini, S. Lepri, R. Livi, and A. Politi, Self-consistent mode-coupling approach to one-dimensional heat transport, *Phys. Rev. E* **73**, 060201 (2006).
- [30] L. Delfini, S. Lepri, R. Livi, and A. Politi, Anomalous kinetics and transport from 1d self-consistent mode-coupling theory, *J. Stat. Mech.* (2007) P02007.
- [31] L. Delfini, S. Denisov, S. Lepri, R. Livi, P. K. Mohanty, and A. Politi, Energy diffusion in hard-point systems, *Eur. Phys. J. Special Topics* **146**, 21 (2007).
- [32] A. Politi, Heat conduction of the hard point chain at zero pressure, *J. Stat. Mech.* (2011) P03028.
- [33] J.J. del Pozo, P.L. Garrido, and P.I. Hurtado, Scaling laws and bulk-boundary decoupling in heat flow, *Phys. Rev. E* **91**, 032116 (2015).
- [34] P.I. Hurtado, Breakdown of hydrodynamics in a simple one-dimensional fluid, *Phys. Rev. Lett.* **96**, 010601 (2006).
- [35] P.I. Hurtado, Strong shock waves and nonequilibrium response in a one-dimensional gas: A Boltzmann equation approach, *Phys. Rev. E* **72**, 041101 (2005).
- [36] G.R. Lee-Dadswell, B.G. Nickel, and C.G. Gray, Thermal conductivity and bulk viscosity in quartic oscillator chains, *Phys. Rev. E* **72**, 031202 (2005).
- [37] G.R. Lee-Dadswell, Predicting and identifying finite-size effects in current spectra of one-dimensional oscillator chains, *Phys. Rev. E* **91**, 012138 (2015).
- [38] S. Liu, P. Hänggi, N. Li, J. Ren, and B. Li, Anomalous heat diffusion, *Phys. Rev. Lett.* **112**, 040601 (2014).
- [39] Y. Li, S. Liu, N. Li, Peter Hänggi, and B. Li, 1D momentum-conserving systems: the conundrum of anomalous versus normal heat transport, *New J. Phys.* **17**, 043064 (2015).
- [40] Special cases as the coupled rotors model, with convergent κ in $1d$ [41, 42], can be also accounted for by fluctuating hydrodynamics [43] after noticing that this model has less than three locally-conserved fields.
- [41] C. Giardinà, R. Livi, A. Politi, and M. Vassalli, Finite thermal conductivity in 1d lattices, *Phys. Rev. Lett.* **84**, 2144 (2000).
- [42] O. V. Gendelman, A. V. Savin, Normal heat conductivity of the one-dimensional lattice with periodic potential of nearest-neighbor interaction, *Phys. Rev. Lett.* **84**, 2381 (2000).
- [43] S.G. Das and A. Dhar, Role of conserved quantities in normal heat transport in one dimension, arXiv:1411.5247 (2014).
- [44] G. Casati, Energy transport and the Fourier heat law in classical systems, *Found. Phys.* **16**, 51 (1986).
- [45] P.L. Garrido and J. Marro, One-dimensional mixtures of hard points with stochastic boundary conditions, *J. Phys. A: Math. Gen.*, **22** 1355 (1989).
- [46] P. L. Garrido, P.I. Hurtado and B. Nadrowski, Simple one-dimensional model of heat conduction which obeys Fourier's law, *Phys. Rev. Lett.* **86**, 5486 (2001).
- [47] A.V. Savin, G.P. Tsironis, and A.V. Zolotaryuk, Heat conduction in one-dimensional systems with hard-point interparticle interactions, *Phys. Rev. Lett.* **88**, 154301 (2002).
- [48] P. Grassberger, W. Nadler, and L. Yang, Heat conduction and entropy production in a one-dimensional hard-particle gas, *Phys. Rev. Lett.* **89**, 180601 (2002).
- [49] G. Casati, L. Wang, and T. Prosen, A one-dimensional hard-point gas and thermoelectric efficiency, *J. Stat. Mech.* (2009) L03004.
- [50] E. Brunet, B. Derrida and A. Gerschenfeld, Fluctuations of the heat flux of a one-dimensional hard particle gas, *Europhys. Lett.* **90**, 20004 (2010).
- [51] A.D. Boozer, Boltzmann equations for a binary one-dimensional ideal gas, *Phys. Rev. E* **84**, 031127 (2011).
- [52] C.B. Mendl, and H. Spohn, Equilibrium time-correlation functions for one-dimensional hard-point systems, *Phys. Rev. E* **90**, 012147 (2014).
- [53] S. Chen, J. Wang, G. Casati, and G. Benenti, Nonintegrability and the Fourier heat conduction law, *Phys. Rev. E* **90**, 032134 (2014).
- [54] J.J. del Pozo, P.L. Garrido, and P.I. Hurtado,

Probing local equilibrium in nonequilibrium fluids, arXiv:1407.3113, submitted to Phys. Rev. E (2015).

- [55] S.M. Bhattacharjee, and F. Seno, A measure of data collapse for scaling, J. Phys. A: Math. Gen. **34**, 6375 (2001).
- [56] P.I. Hurtado and P.L. Garrido, to be published.
- [57] P. Cipriani, S. Denisov, and A. Politi, From Anomalous Energy Diffusion to Lévy Walks and Heat Conductivity in One-Dimensional Systems, Phys. Rev. Lett. **94**, 244301 (2005).
- [58] A. Dhar, K. Saito, and B. Derrida, Exact solution of a Lévy walk model for anomalous heat transport, Phys. Rev. E **87**, 010103(R) (2013).
- [59] C. Bernardin, P. Gonçalves, and M. Jara, 3/4-superdiffusion in a system of harmonic oscillators perturbed by a conservative noise, arXiv:1402.1562 (2014).
- [60] M. Jara, T. Komorowski, and S. Olla, Superdiffusion of energy in a chain of harmonic oscillators with noise, arXiv:1402.2988 (2014).

APPENDIX A

Scaling in Fourier's law

In this Appendix we will show that the stationary density and temperature profiles of the $1d$ diatomic hard-point fluid driven out of equilibrium by an arbitrary temperature gradient follow from an universal master curve, provided that three simple hypotheses hold (see below). It will be then trivial to show that the reverse statement also holds true, i.e. that a nonequilibrium $1d$ fluid whose density and temperature profiles collapse onto an universal master curve is bounded to obey the three mentioned properties. These hypotheses are:

- (i) **Fourier's law:** In the steady state, the nonequilibrium fluid sustains a non-vanishing heat current J proportional to the temperature gradient

$$J = -\kappa_L(\rho, T) \frac{dT(x)}{dx}, \quad x \in [0, L], \quad (4)$$

with $\kappa_L(\rho, T)$ a well-defined local conductivity functional which may depend on L .

- (ii) **Macroscopic local equilibrium (MLE):** This amounts to assume that local thermodynamic equilibrium holds at the macroscopic level, in the sense that the local density and temperature are related by the *equilibrium* equation of state (EoS) [54]. For the $1d$ diatomic hard-point gas studied in this paper, it is simply the ideal gas EoS

$$P = \rho T, \quad (5)$$

with P the fluid's pressure.

- (iii) **Heat conductivity scaling:** Due to the homogeneity of the interaction potential, the heat conductivity of the $1d$ diatomic hard-point gas exhibits a well-known density temperature separability [33]. Moreover, standard dimensional analysis arguments show that $\kappa \propto \sqrt{T/m}$ [33], and the

known dimensional anomaly for transport implies in turn that $\kappa \propto L^\alpha$ at leading order. We now raise these arguments to a formal scaling ansatz

$$\kappa_L(\rho, T) = L^\alpha \sqrt{T/m} k(\rho), \quad (6)$$

with $k(\rho)$ a function solely dependent on density. Note that this ansatz discards possible subleading corrections in L .

We may now use the MLE property (ii) and the conductivity scaling ansatz (iii) to write Fourier's law in terms only of the density field. In particular, using the EoS to write $T(x) = P/\rho(x)$, we obtain

$$\frac{J\sqrt{m}}{P^{3/2}} L^{-\alpha} = G'(\rho) \frac{d\rho}{dx} = \frac{dG(\rho)}{dx}, \quad (7)$$

where $G'(\rho) \equiv k(\rho)\rho^{-5/2}$ and $'$ denotes derivative with respect to the argument. This equation, together with the boundary conditions for the density field, $\rho(x=0, L) = \rho_{0,L}$, which can be inferred from the constraints

$$\frac{T_0}{T_L} = \frac{\rho_L}{\rho_0}, \quad (8)$$

$$\eta = \frac{1}{L} \int_0^L \rho(x) dx = \frac{\int_{\rho_0}^{\rho_L} \rho G'(\rho) d\rho}{G(\rho_L) - G(\rho_0)}, \quad (9)$$

completely define the macroscopic problem in terms of $\rho(x)$. Note that the externally controlled parameters in the problem are the temperatures of the boundary reservoirs, $T_{0,L}$, and the global number density η . The pressure and the heat current can be now obtained as $P = T_0 \rho_0$ and $J = P^{3/2} [G(\rho_L) - G(\rho_0)] / (L^{1-\alpha} \sqrt{m})$.

A simple yet striking consequence of hypotheses (i)-(iii) can be now directly inferred from Eq. (7). In fact, as both J and P are state-dependent constants, this immediately implies that $G[\rho(x)] = \psi L^{-\alpha} x + \zeta$, i.e. $G[\rho(x)]$ is a linear function of position $x \in [0, L]$, with $\psi = J\sqrt{m}/P^{3/2}$ the reduced current and $\zeta = G(\rho_0)$ a constant. Equivalently,

$$\rho(x) = F\left(\frac{\psi}{L^\alpha} x + \zeta\right), \quad (10)$$

where we have assumed that the function $G(\rho)$ has a well-defined inverse $F(u) \equiv G^{-1}(u)$. This assumption seems reasonable as steady density profiles are typically well behaved and readily measurable in simulations and experiments, see e.g. Fig. 1 in the main text. Therefore, according to Eq. (10), there exists a single universal master curve $F(u)$ from which any steady state density profile follows after a linear spatial scaling $x = L^\alpha(u - \zeta)/\psi$. This scaling behavior is automatically transferred to temperature profiles via the local EoS $P = \rho(x)T(x)$, so

$$\frac{T(x)}{P} = \frac{1}{F\left(\frac{\psi}{L^\alpha} x + \zeta\right)}. \quad (11)$$

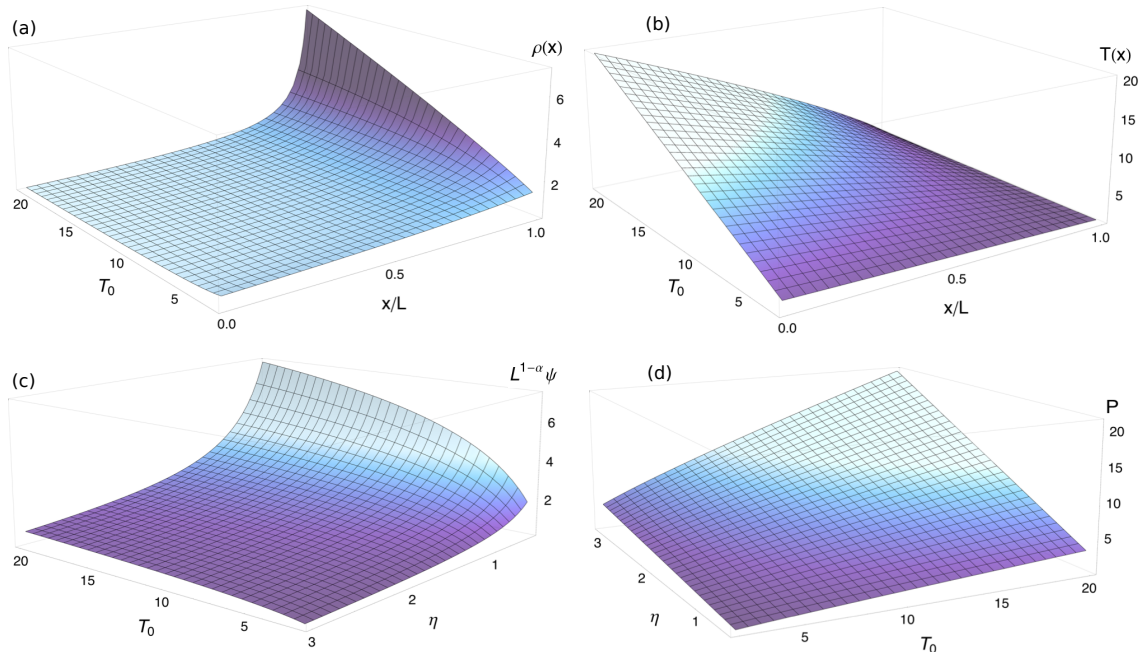


FIG. 6. (Color online) Density (a) and temperature (b) profiles as a function of T_0 for $\eta = 1$, obtained from the full solution of the macroscopic heat transport problem for the $1d$ diatomic hard-point gas, see Eq. (13) and the associated discussion. Also shown are the η - and T_0 -dependence of (c) the scaled reduced current, $L^{1-\alpha}\psi$, and (d) the nonequilibrium fluid's pressure P , see Eqs. (15)-(16). All these curves are for a mass ratio $\mu = 3$, for which $\alpha = 0.297(6)$ and $a = 1.1633(9)$, see Table I below.

These scaling laws are independent of the global density η or the nonequilibrium driving defined by the baths temperatures T_0 and T_L , depending exclusively on the function $k(\rho)$ controlling the fluid's heat conductivity. Alternatively, Eq. (10) implies that any measured steady density profile can be collapsed onto the universal master curve $F(u)$ by scaling space by the scaled reduced current $L^{-\alpha}J\sqrt{m}/P^{3/2}$ measured in each case and shifting the resulting profile an arbitrary constant ζ (similarly for temperature profiles). This suggests a simple scaling method to obtain the universal master curves in simulations or experiments, a procedure that we implement in the main text. Note that these results are not limited to the $1d$ diatomic hard-point gas; equivalent results hold for general d -dimensional (non-critical) fluids driven arbitrarily far from equilibrium, see Ref. [33] for a proof.

Proving the reverse statement, i.e. that a $1d$ fluid obeying Eqs. (10)-(11) does fulfill also properties (i)-(iii) above, is now trivial. In particular, the MLE property (ii) is automatically satisfied by construction. Moreover, inverting the scaling in (10) to obtain $G[\rho(x)]$ and differentiating this functional with respect to x we arrive at $J = -L^\alpha \sqrt{T/m} G'(\rho) \rho^{5/2} T'(x)$, where we used that $T(x) = P/\rho(x)$, see Eqs. (10)-(11). This hence proves that properties (i) and (iii) also hold, with a heat conductivity given by Eq. (6) with $k(\rho) = G'(\rho)\rho^{5/2}$.

The combination of our scaling ansatz for the heat conductivity and well-known dynamical invariances of $1d$ hard point fluids under scaling of different magnitudes (as e.g. temperature, velocities, mass, space, etc.) re-

sults in a well-defined density dependence for the heat conductivity, see main text, namely $k(\rho) = a\rho^\alpha$, with a a constant of $\mathcal{O}(1)$. Such power-law dependence, which reflects the transport anomaly, is fully confirmed in local measurements of the density dependence of κ_L , see Appendix B below, from which we obtain precise estimates of the amplitude $a(\mu)$, see Table I. Such clear-cut observation, together with the scaling formalism described above, allows now for a complete solution of the *macroscopic* transport problem for this model, written in terms of the external control parameters, namely T_0, T_L, η and L , together with α and a . In fact, recalling that $G'(\rho) = k(\rho)\rho^{-5/2}$ we obtain that $G(\rho) = \nu^*(1 - \rho^{\alpha-3/2})$, with $\nu^* \equiv a/(\frac{3}{2} - \alpha)$ and where we have chosen an arbitrary constant such that $F(0) = 1 = G^{-1}(0)$. The universal master curve hence reads

$$F(u) = \left(1 - \frac{u}{\nu^*}\right)^{\frac{2}{2\alpha-3}}. \quad (12)$$

This prediction is compared with the measured master curves in Fig. 4 of the main text, and the agreement is excellent for all mass ratios μ . Eq. (12) implies in turn that density profiles can be written as

$$\rho(x) = \left[\left(\frac{P}{T_0}\right)^{\alpha-\frac{3}{2}} - \frac{\psi}{\nu^*} L^{-\alpha} x \right]^{\frac{2}{2\alpha-3}}, \quad (13)$$

while temperature profiles simply follow from $T(x) = P/\rho(x)$, namely

$$T(x) = \left[T_0^{\frac{3}{2}-\alpha} - \frac{J\sqrt{m}}{\nu^* P^\alpha} L^{-\alpha} x \right]^{\frac{2}{3-2\alpha}}. \quad (14)$$

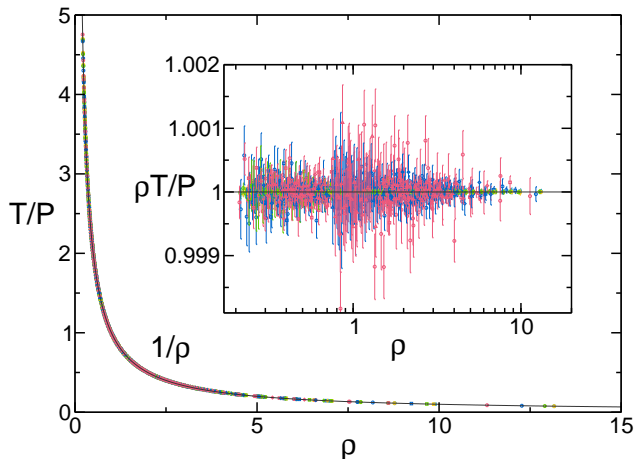


FIG. 7. (Color online) Measured local reduced temperature, $T(x)/P$, plotted as a function of the associated local density $\rho(x)$ for $\mu = 3$ and $\forall T_0, \eta, N$, corresponding to all profiles displayed in Fig. 1 of the paper and summing up to 2400 data points from 80 different simulations. An excellent data collapse is obtained which follows with high precision the expected ideal-gas behavior $1/\rho$, plotted as a thin line. Inset: Scaling plot of $\rho(x)T(x)/P$ vs $\rho(x)$ for the same conditions. These data show that macroscopic local equilibrium is a very robust property, even in the presence of strong finite-size corrections on the hydrodynamic profiles.

The calculation is completed by expressing the heat current J and the pressure P in terms of the external parameters by using Eqs. (8)-(9) above. This yields

$$P = \eta \left(\frac{\frac{1}{2} - \alpha}{\frac{3}{2} - \alpha} \right) \left(\frac{T_0^{3/2-\alpha} - T_L^{3/2-\alpha}}{T_0^{1/2-\alpha} - T_L^{1/2-\alpha}} \right), \quad (15)$$

$$J = \frac{a\eta^\alpha \left(\frac{1}{2} - \alpha\right)^\alpha}{L^{1-\alpha} \sqrt{m} \left(\frac{3}{2} - \alpha\right)^{1+\alpha}} \frac{(T_0^{3/2-\alpha} - T_L^{3/2-\alpha})^{1+\alpha}}{(T_0^{1/2-\alpha} - T_L^{1/2-\alpha})^\alpha} \quad (16)$$

The last equation for the current can be rewritten as $J = \eta^\alpha L^{\alpha-1} m^{-1/2} T_L^{3/2} h_\alpha(T_0/T_L)$, with

$$h_\alpha(z) \equiv a \frac{\left(\frac{1}{2} - \alpha\right)^\alpha}{\left(\frac{3}{2} - \alpha\right)^{1+\alpha}} \frac{(z^{3/2-\alpha} - 1)^{1+\alpha}}{(z^{1/2-\alpha} - 1)^\alpha}. \quad (17)$$

These predictions are fully confirmed by simulations data, see main text. As a self-consistent check, note that in the equilibrium limit $T_0 \rightarrow T_L$ both the pressure and the heat current converge to their expected value, namely $P = \eta T_L$ and $J = 0$. Fig. 6 shows the density and temperature profiles predicted for a *macroscopic* diatomic hard-point fluid as a function of T_0 for $\eta = 1$, as well as the pressure and the scaled reduced current $L^{-\alpha}\psi$ as a function of T_0 and η . These plots are obtained for a particular mass ratio $\mu = 3$, for which $\alpha = 0.297(6)$ and $a = 1.1633(9)$, see Table I below, and yield an excellent comparison with simulation data, see Fig. 1 in the main text and Fig. 8 in Appendix B.

Interestingly, the master curve $F(u)$ obtained above exhibits a vertical asymptote at $u = \nu^*$, see Eq. (12),

and this implies in turn the existence of a maximal scaled reduced current ψ^* . Indeed, for the associated density profile to exist in its whole domain $x \in [0, L]$, see Eq. (13), the following condition must hold

$$\psi \leq \frac{\nu^*}{L^{1-\alpha}} \left(\frac{T_0}{P} \right)^{3/2-\alpha} \equiv \frac{\psi^*}{L^{1-\alpha}}, \quad (18)$$

with P expressed as in Eq. (15). This defines a maximal scaled reduced current ψ^* , such that the scaled current $L^{1-\alpha}J \leq \psi^* P^{3/2}/\sqrt{m} = \nu^* T_0^{3/2-\alpha} P^\alpha/\sqrt{m} \forall T_0, T_L, \eta, L$, defining an upper bound on the heat current in terms of the nonequilibrium pressure. The maximal scaled reduced current increases monotonously with T_0 , saturating to an asymptotic value in the $T_0 \rightarrow \infty$ limit, namely

$$\psi^* \xrightarrow{T_0 \rightarrow \infty} \frac{a \left(\frac{3}{2} - \alpha\right)^{1/2-\alpha}}{\left[\eta \left(\frac{1}{2} - \alpha\right)\right]^{3/2-\alpha}}. \quad (19)$$

Note however that both $L^{1-\alpha}J$ and P diverge as $T_0 \rightarrow \infty$, though ψ^* remains finite.

To end this section, we remark that Eqs. (12)-(16) constitute the solution of the *macroscopic* transport problem for this model. A comparison of the predicted density and temperature profiles, see Eqs. (13)-(14), with the finite-size data of Fig. 1 in the main text will allow us below to investigate the bulk-boundary decoupling phenomenon in detail by quantifying the jump between the effective boundary conditions imposed by the boundary layers on the bulk fluid and the empirical bath temperatures.

APPENDIX B Some additional results

In this Appendix we provide additional data, obtained from our extensive simulations of the $1d$ diatomic hard-point fluid model, which support our conclusions in the main text.

Our first goal is to test the macroscopic local equilibrium (MLE) property directly from our data. As described above, MLE conjectures that local thermodynamic equilibrium holds at the macroscopic level, in the sense that the stationary density and temperature fields are locally related by the *equilibrium* equation of state (EoS) [54], which for this model is simply the ideal gas EoS,

$$P = \rho(x)T(x). \quad (20)$$

In order to test MLE, we hence take the density and temperature profiles of Fig. 1 measured for $\mu = 3$ and different T_0, N, η , and plot in Fig. 7 the local reduced temperature, $T(x)/P$, with P the finite-size pressure measured in each simulation, as a function of the associated local

density $\rho(x)$. All data, comprising 2400 points from 80 different simulations for widely different systems sizes, temperature gradients and global densities, collapse onto a single curve which follows with high precision the expected ideal-gas behavior $1/\rho$, see line in Fig. 7 and inset therein. Note that, interestingly, the excellent data collapse is maintained also for points within the boundary layers near the thermal walls. Moreover, similar results hold for all mass ratios μ studied in this paper. In this way, the observed high-precision data collapses confirm the robustness of the MLE property far from equilibrium [54], even in the presence of important finite size effects, validating in an independent manner one of the hypotheses underlying the scaling picture of Appendix A.

In addition to density and temperature profiles, see Fig. 1 in the main text, we also measured in our simulations the nonequilibrium fluid's pressure P and the heat current J flowing through the system (both in the bulk and at the thermal walls). These observables are necessary in order to scale the spatial coordinate of the hydrodynamic profiles using the measured reduced current $\psi = J\sqrt{m}/P^{3/2}$ in each case. Fig. 8 shows the measured P (a) and ψ (b) as a function of T_0 and η for $\mu = 3$ and different system sizes N . These data refer to wall observables, though the associated bulk observables yield completely equivalent results (as otherwise expected). The comparison of these data with our predictions in Appendix A is excellent, see Fig. 6 above.

We next focus on the density dependence of the heat conductivity as parametrized by $k(\rho)$. One can easily show that $k(\rho) = J\sqrt{m}[L^\alpha \sqrt{T(x)}|T'(x)|]^{-1}$, so for each set (N, T_0, η) and fixed μ we performed discrete derivatives of the measured bulk temperature profile to evaluate $T'(x)$ and plotted the previous expression, with J measured in each case, as a function of the associated $\rho(x)$. Fig. 9 shows the curves $k(\rho)$ so obtained for different μ , which display the best collapse when the measured exponent $\alpha(\mu)$ is used. Interestingly the resulting scaling functions, though somewhat noisy due to discretization effects, exhibit a clear power-law behavior, $k(\rho) = a\rho^\beta$, and the fitted exponent is fully compatible in all cases with the measured anomaly exponent, $\beta = \alpha(\mu)$, see Fig. 3 in main text and Table I below. These measurements prove in an independent way that the heat conductivity of the diatomic hard-point gas does depend indeed on the local density (in addition to the expected $\sqrt{T/m}$ -dependence). The observed power-law behavior, which reflects the transport anomaly, is then expected on the basis of the scaling symmetries of the dynamics of 1d hard-point fluids, see the main text and Appendix A.

As described previously, we can use that $k(\rho) = a\rho^\alpha$ to solve the macroscopic transport problem for the 1d diatomic hard-point fluid. A main prediction of this solution is the form of temperature (and density) profiles for arbitrary external conditions, see Eqs. (13)-(14). To test these predictions, we plot $T(x)^{3/2-\alpha}$ vs x , with $T(x)$

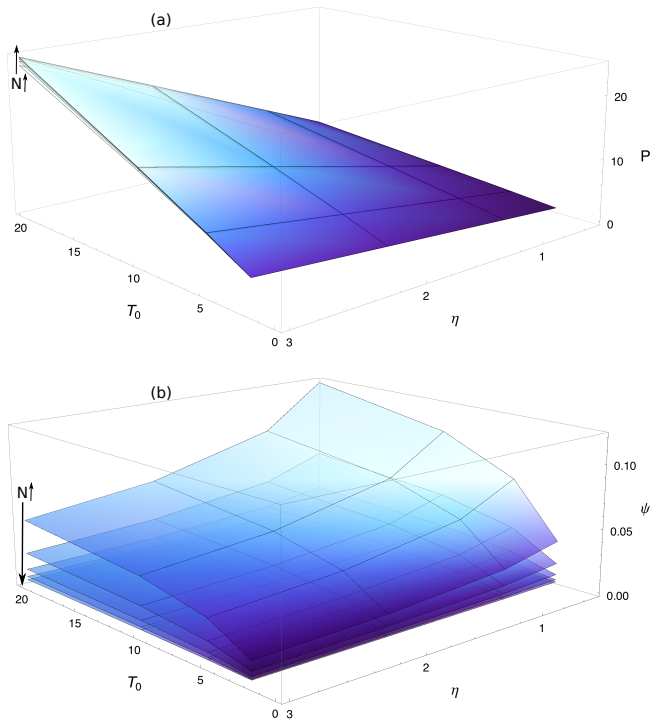


FIG. 8. (Color online) Measured pressure P (a) and reduced current $\psi = J\sqrt{m}/P^{3/2}$ (b) as a function of T_0 and η for $\mu = 3$ and different system sizes N . Data here refer to wall observables, though the associated bulk observables yield completely equivalent results.

the measured temperature profiles for each μ , N , η and T_0 . This is predicted to be a straight line with slope $-(3/2 - \alpha)JL^{1-\alpha}\sqrt{m}/(aP^\alpha)$, with J and P the measured current and pressure, respectively. Such linear dependence is confirmed for bulk temperature profiles in all cases, with the correct slope, and with the y -intercept of the line as only fitting parameter (similar results hold also for density profiles). Fig. 10 shows an example of this test for $\mu = 3$, $\eta = 1$, varying $T_0 \in [2, 20]$ and two different system sizes, $N = 101$ (small) and $N = 10001$ (large), with excellent agreement in all cases. The fitted y -intercept yields the effective $T_0^{(\text{ef})3/2-\alpha}$ for each profile, and this together with the predicted slope yields the effective $T_L^{(\text{ef})}$. These effective boundary temperatures slightly differ from the thermal wall temperatures in each case, $T_{0,L}^{(\text{ef})} \neq T_{0,L}$. In this way, the measured *bulk* temperature (and density) profiles for any finite N are in fact those of a *macroscopic* diatomic hard-point gas obeying (1) but subject to some effective, N -dependent boundary conditions controlled by the boundary layers. This is a manifestation of the bulk-boundary decoupling phenomenon already reported in hard disks out of equilibrium [33], which enforces the macroscopic laws on the bulk of the finite-sized fluid.

Using the previous approach, we measured the effective $T_{0,L}^{(\text{ef})} \forall \mu, N, \eta$ and T_0 . As shown in the main text, these

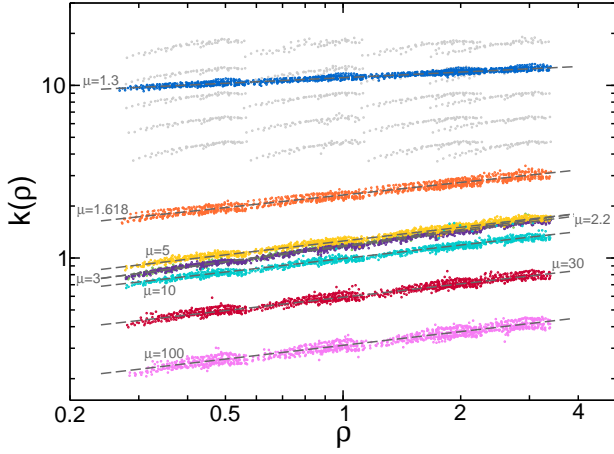


FIG. 9. (Color online) Density dependence of heat conductivity as captured by $k(\rho)$. Light gray points show the curves obtained for $\mu = 3$ before scaling data by $L^{-\alpha}$ along the y -axis, while dark color curves show the scaled curves for each μ . A power-law behavior is apparent in all cases. Dashed lines are power-law fits to the data, see main text.

μ	α	β	a
1.3	0.108 (9)	0.109 (1)	11.105 (8)
1.618	0.242 (23)	0.2408 (18)	2.307 (3)
2.2	0.308 (5)	0.3068 (11)	1.1765 (9)
3	0.297 (6)	0.2964 (11)	1.1633 (9)
5	0.266 (11)	0.2641 (12)	1.2622 (12)
10	0.260 (14)	0.2632 (19)	0.9874 (14)
30	0.258 (18)	0.257 (1)	0.5942 (12)
100	0.265 (22)	0.2648 (23)	0.3095 (5)

TABLE I. Measured values of the anomaly exponent α and its error for different mass ratios μ , see Fig. 3. Also shown are the fitted exponent and amplitude of the power-law density dependence of the conductivity, $k(\rho) = a\rho^\beta$, see Fig. 5. Notice that in all cases $\beta = \alpha$ within error bars.

effective boundary conditions can now be used in turn to test the theoretical prediction for the current in terms of the external parameters, see Eqs. (16)-(17), and we find an excellent agreement in all cases, see Fig. 5 in the main text.

Finally, Table I summarizes the values of the anomaly exponent α as a function of the mass ratio μ measured from the optimal collapse of scaled density profiles, see Figs. 2-3. Table I also displays, for each μ , the exponent β and amplitude a of the power-law fit to the density dependence of the conductivity, $k(\rho) = a\rho^\beta$, see Fig. 5 in the paper. In all cases $\beta \approx \alpha$, and errors are included in all measurements.

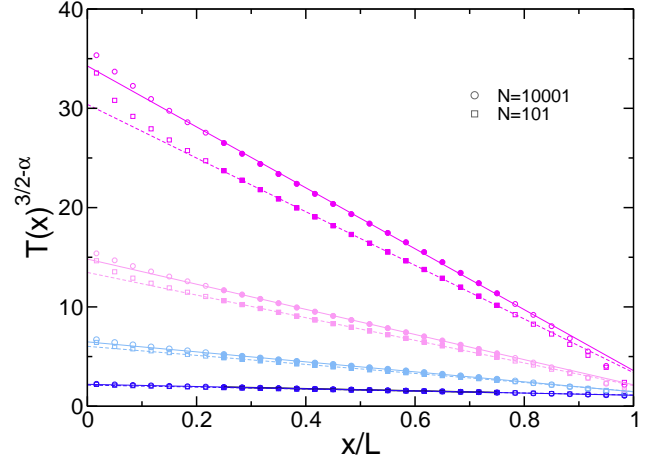


FIG. 10. (Color online) Measured temperature profiles to the power $(3/2 - \alpha)$ vs x , for $\mu = 3$, $\eta = 1$, varying $T_0 \in [2, 20]$ and two different system sizes, $N = 101$ (\square) and $N = 10001$ (\circ), small and large. Filled symbols correspond to the bulk, while open symbols signal the boundary layers. Lines have slope $-(3/2 - \alpha)JL^{1-\alpha}\sqrt{m}/(aP^\alpha)$, with J and P the measured current and pressure in each case, and the only fitting parameter corresponds to the y -intercept, which yields $T_0^{(\text{ef})3/2-\alpha}$ in each case. Note that $T_L^{(\text{ef})}$ follows from $T_0^{(\text{ef})}$ and the (fixed) slope. The agreement between lines and data confirm that *bulk* temperature (and density) profiles for any finite N are in fact those of a *macroscopic* diatomic hard-point gas subject to some effective, N -dependent boundary conditions controlled by the boundary layers. For $\mu = 3$, recall that $\alpha = 0.297(6)$ and $a = 1.1633(9)$, see Table I below.

APPENDIX C

A metric to quantify data collapse

In this section we briefly explain the standard metric used in this work to quantify data collapse. This metric is based on the collapse distance first proposed in Ref. [55] and widely used in physics literature, in particular in order to obtain scaling exponents via a distance minimization procedure.

We hence consider a set of K curves, each one containing M points, and we denote this set as $\{(x_i^{(k)}, y_i^{(k)}), i \in [1, M], k \in [1, K]\}$. The idea is now to choose an arbitrary curve $\bar{k} \in [1, K]$ as reference curve, and proceed to measure the distance of all other curves $k \neq \bar{k}$ to this reference curve along the x -direction. For that we measure the distance between each point in k and the interpolated point in \bar{k} with the same y -coordinate. In order to do so, we have to restrict to points in k overlapping with the reference curve \bar{k} . Note also that we choose to measure distances only along the x -direction because the scaling approach developed in this paper only affects the x -coordinates of the measured curves, see Appendix A and Figs. 2 and 4 in the main text. Moreover, since the chosen reference curve \bar{k} is completely arbitrary, we repeat this procedure for all curves as reference curve, and

average the resulting distances. In this way, our collapse metric is defined as [55]

$$D \equiv \frac{1}{\ell_{\max} \mathcal{N}_{\text{overl}}} \sum_{\bar{k}=1}^K \sum_{\substack{k=1 \\ k \neq \bar{k}}}^K \sum_{\substack{i=1 \\ i \text{ overlap } \bar{k}}}^M \left| x_i^{(k)} - \bar{x}_i^{(k, \bar{k})} \right|, \quad (21)$$

where $\bar{x}_i^{(k, \bar{k})}$ is the (interpolated) x -coordinate of a point in curve \bar{k} with y -coordinate equal to $y_i^{(k)}$, i.e. the projection of point $(x_i^{(k)}, y_i^{(k)})$ of curve k on curve \bar{k} along the x -axis. The innermost sum over i in Eq. (21) is restricted to points in curve k which overlap with curve \bar{k} along the y -direction, i.e. those points in k whose y -coordinate is between the minimum and maximum y -coordinate of curve \bar{k} . In order to obtain now the projection $\bar{x}_i^{(k, \bar{k})}$ in Eq. (21) any interpolation scheme can be used, though for our purposes the simplest linear interpolation works well. In particular, we choose

$$\bar{x}_i^{(k, \bar{k})} = \frac{y_i^{(k)} - B_i^{(k, \bar{k})}}{A_i^{(k, \bar{k})}}, \quad (22)$$

with $A_i^{(k, \bar{k})}$ and $B_i^{(k, \bar{k})}$ the slope and the y -intercept of the interpolating function,

$$A_i^{(k, \bar{k})} = \frac{y_{i_+}^{(\bar{k})} - y_{i_-}^{(\bar{k})}}{x_{i_+}^{(\bar{k})} - x_{i_-}^{(\bar{k})}},$$

$$B_i^{(k, \bar{k})} = \frac{y_{i_+}^{(\bar{k})} x_{i_-}^{(\bar{k})} - y_{i_-}^{(\bar{k})} x_{i_+}^{(\bar{k})}}{x_{i_+}^{(\bar{k})} - x_{i_-}^{(\bar{k})}}.$$

The points $(x_{i_{\pm}}^{(\bar{k})}, y_{i_{\pm}}^{(\bar{k})})$ correspond to the points in the \bar{k} -curve bracketing point i of k -curve along the y -direction, see sketch in Fig. 11. To normalize the distance metric, we divide the resulting sums by the total number of overlapping points, $\mathcal{N}_{\text{overl}}$. Moreover, because the $L^{-\alpha}$ scaling in the x -coordinate of the measured density and temperature profiles may affect strongly the total span of the collapsed curves depending on the anomaly exponent α used, the collapse metric is also normalized by the total

span in the x -direction of the curve cloud, $\ell_{\max} \equiv (x_{\max} - x_{\min})$ with $x_{\max} = \max_{k,i} \{x_i^{(k)}\}$, $i \in [1, M]$, $k \in [1, K]$ and $x_{\min} = \min_{k,i} \{x_i^{(k)}\}$, $i \in [1, M]$, $k \in [1, K]$, i.e. our distance is relative to the total span of the curve cloud in the x -direction.

In order to obtain the exponent α characterizing anomalous Fourier's law in our $1d$ fluid, we minimize the metric (21) for varying mass ratios μ . In fact, the collapse metric $D(\alpha, \mu)$ exhibits a deep and narrow minimum as a function of α for each μ , see inset to Fig. 3 in the main text, offering a precise measurement of the anomaly exponent. Moreover, an estimate of the exponent error can be obtained from the width and depth of this minimum [55]. By expanding $\ln D(\alpha, \mu)$ around the minimum at $\alpha = \alpha_0$, the width can be estimated as [55]

$$\Delta\alpha = \frac{\epsilon\alpha_0}{\sqrt{2 \ln \left[\frac{D(\alpha_0 \pm \epsilon\alpha_0, \mu)}{D(\alpha_0, \mu)} \right]}}, \quad (23)$$

for a given level ϵ . Here we choose $\epsilon = 0.01$, so the estimate for the anomaly exponent is $\alpha_0 \pm \Delta\alpha$ with an errorbar reflecting the width of the minimum at the 1% level [55].

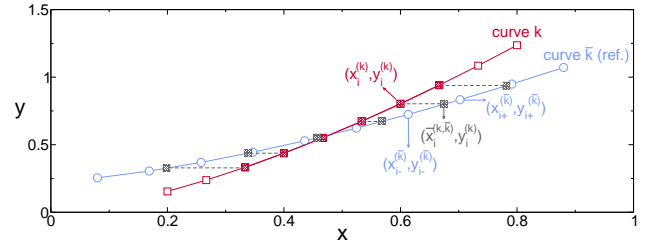


FIG. 11. (Color online) Sketch explaining the metric used to quantify data collapse, see Eq. (21). This metric estimates the distance between a curve k (\square) and the reference curve \bar{k} (\circ) by measuring the average distance between each point in k and the interpolated point in \bar{k} with the same y -coordinate (gray, shaded squares). Note that we restrict to points in k overlapping with the reference curve \bar{k} , see filled squares. The distance corresponds in this example to the average length of the dashed segments.